Advances in Applied Mathematics and Mechanics
Adv. Appl. Math. Mech., Vol. **10**, No. 2, pp. 390-408

DOI: 10.4208/aamm.OA-2017-0126
April 2018

# Numerical Investigation of Multiple Shock/ Turbulent Flow Interaction in a Supersonic Channel

Peizhao Sun, Jiming Yang and Xiyun Lu[1,*]

[1] *Department of Modern Mechanics, University of Science and Technology of China, Hefei, Anhui 230026, China*

Received 11 May 2017, Accepted (in revised version) 8 July 2017

**Abstract.** Numerical investigation of multiple shock/turbulent flow interaction is carried out using large eddy simulation for a supersonic channel flow with an inlet free stream Mach number 1.61. Various fundamental mechanisms dictating the flow phenomena including shock train, shear layer and turbulence behavior are investigated. It is found that the existence of the shock train and separated shear layer has an important influence on turbulence features. The turbulence intensities and turbulent kinetic energy (TKE) are strengthened in the region of the multiple shock because of the unsteadiness of the shocks. The investigation on the transport equations of the TKE and the pressure fluctuation reveals that the multiple shock and the roll-up vortices of shear layer can promote the generation of the TKE and the pressure fluctuation. The unsteady behavior of flow field is further analyzed by means of the proper orthogonal decomposition method. It is found that the multiple shock and the separated shear layer dominate the unsteady feature.

**AMS subject classifications**: 76F65, 76L05, 76F70

**Key words**: Large eddy simulation, shock train, turbulent flow.

## 1 Introduction

The characteristics of shock wave/boundary layer interaction for the external flows have been widely investigated [1–5]. Nevertheless, the multiple shock wave/boundary layer interaction for the internal flows is more complicated. The shock train or pseudo-shock structure will form in a variety of devices, such as the straight ducts, diffusers and nozzles [6]. The features of the shock train and multiple shock wave/boundary layer interaction are mainly dependent on the incoming Mach number and the flow confinement [6].

*Corresponding author.
*URL:* `http://staff.ustc.edu.cn/~xlu/`
*Emails:* pzsun@mail.ustc.edu.cn (P. Z. Sun), jmyang@ustc.edu.cn (J. M. Yang), xlu@ustc.edu.cn (X. Y. Lu)

 

Based on previous studies [6–8], the interaction between normal shock and boundary layer in the internal flow can be divided into four categories. When the incoming Mach number is supersonic and less than 1.2, the strength of the shock is too weak to induce the boundary layer separation. In this situation, the shock is straight and similar to an inviscid normal shock. When the incoming Mach number increases to 1.2$\sim$1.3, the shock is enhanced to become curve, which is still similar to an inviscid shock. If the incoming Mach number increases again, the shock becomes stronger and induces the boundary layer separation. The separation in turn leads to the bifurcation of the shock. If the incoming Mach number is greater than 1.5, more shocks occur and the shock strain forms.

If the separation caused by the first shock is strong enough, a low-frequency oscillation can be observed [7], which is similar to the breathing motion of the separation bubble in the shock wave/boundary layer interaction [3]. For the shock train structure, the first shock and following shocks all have oscillation phenomena and the oscillation amplitude is enhanced with the increase of the incoming Mach number [7]. The mechanism relevant to the oscillation is still unclear [7–11]. Ikui [7] conducted an experiment in a straight pipe and analyzed the oscillation phenomena of the shocks with the small disturbances upstream the shock. The following experiments [9, 10] indicated that the oscillation is induced by the upstream propagation of the pressure fluctuation along the subsonic region in the downstream of duct. Sugiyama [11] also pointed out that the separation caused by the first shock may be a reasonable explanation of the oscillation of shock train.

The investigation on the shock wave/boundary layer interaction of the internal flow was first conducted for the purpose of designing the supersonic wind tunnels [12]. Then, it is found that the shock train structure is different from the single shock wave/boundary layer interaction [13, 14] and this problem is also studied by numerical simulation and experiment [6]. Among these investigations, the experiments conducted by Carroll [15–18] are prominent. The experiment utilized LDV to collet detailed turbulence statistics in the flow field, which is chosen in this paper for validation.

The numerical simulations of the shock train problem are mainly conducted by means of RANS. Early studies [18–21] used Baldwin-Lomax algebraic model, followed by simulations [22,23] with $k$–$\epsilon$ model, while they all exhibited poor agreement with experimental data. During recent years, some high-fidelity simulations are available [24–26]. Boles [24] conducted a simulation of inlet/isolator configuration with the incoming Mach number $Ma=5$. The hybrid large-eddy simulation (LES)/Reynolds average Navier-Stokes (RANS) model is utilized and a bigger separation region and a stronger shock train structure are observed with respect to experimental result. Koo [25] simulated the unstart process of the inlet/isolator model and over-predicted the separation and the propagation velocity of the unstart shock. Morgan [26] investigated the normal shock train using LES. Although the Reynolds number is lower than that in the experiment, a good agreement of the shock train structure and the quantitative results with experimental data is observed. While for the situation with periodic condition in the spanwise, the position of the shock train is relatively backward with respect to experimental result.

In this paper, an LES technique, which has provided a powerful tool for studying the dynamics of turbulent flows, is utilized to investigate the normal shock train in a supersonic channel with a free stream Mach number 1.61. The purpose is to achieve an improved understanding of some fundamental phenomena and statistical properties of the internal flow. This paper is organized as follows. A description of the computational model is presented in Section 2. Detailed results are then given in Section 3 and concluding remarks are addressed in Section 4.

# 2 Computational model

## 2.1 Mathematical formulation and numerical procedure

To investigate the internal flow inside a supersonic channel, the three-dimensional Favre-filtered compressible Navier-Stokes equations in generalized coordinates are employed. The equation of state for an ideal gas is used and the molecular viscosity is assumed to obey the Sutherland law. The equations are non-dimensionalized by means of the free stream variables, including the density $\rho_\infty$, temperature $T_\infty$, speed of sound $a_\infty$ and characteristic scale $\delta$ which is the 99% velocity thickness of the inflow boundary layer.

The LES is implemented in the present work for turbulence closure. Some terms in the Favre-filtered equations arise from unsolved scales and need to be modelled in terms of resolved scales. Then, dynamic subgrid-scale models for compressible flows are employed. A detailed description of the mathematical formulation of the nondimensionalized equations and the subgrid-scale models can be found in our previous papers [27–30].

In this study, inflow boundary conditions are presented as follows. The inflow boundary condition is handled using an artificially synthesized approach [31, 32] which is extensively tested in previous literatures [33, 34, 36]. The average inflow velocity profile is generated from the results of RANS. The velocity disturbances at the inlet are determined and the random velocity fluctuations with a maximum amplitude 4% of the free-stream velocity are added to the velocity components [33–36].

## 2.2 Computational overview and validation

As shown in Fig. 1, a typical configuration is considered here with free-stream Mach number $M_{in}=1.61$. The total pressure and total temperature at the inflow condition are $P_0=206K$Pa and $T_0=295K$, respectively. The 99% velocity thickness $\delta$ of the inflow boundary layer is 5.4mm, which results in a confinement parameter ($\delta/h$) of 0.32. The unit Reynolds number based on the 99% velocity thickness is $1.62\times 10^5$ [16].

To perform the numerical simulation, the computational domain is discretized by equally spaced grids in the streamwise $(x)$ and spanwise $(y)$ directions and a stretched grid in the wall-normal direction $(z)$, so that there are enough points near the two walls to capture the boundary layer information. Based on careful examination, the computational domain is used as $-20\le x\le 54$ in the streamwise direction, $0\le z\le 6.25$ in the vertical direction and $-1.5\le y\le 1.5$ in the spanwise direction. The coordinates $x$, $y$ and

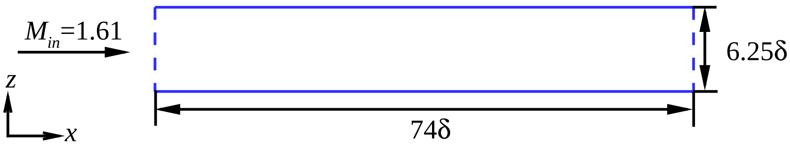


Figure 1: Schematic of the channel model.

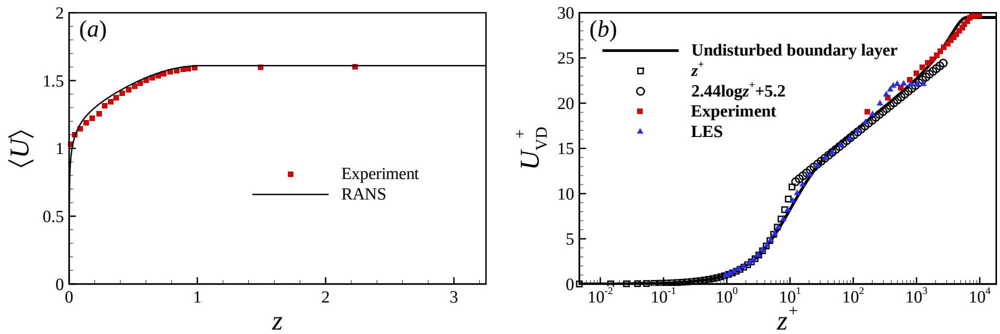


Figure 2: Distributions of (a) mean streamwise velocity calculated by RANS and (b) van Driest transformed mean streamwise velocity in the undisturbed incoming boundary layer. The experimental data comes from Carroll et al. [16] and the LES result from Morgan et al. [26].

$z$ are nondimensionalized by the velocity thickness $\delta$ of the inflow boundary layer. The periodic condition is employed in the spanwise direction. The no-slip, adiabatic wall condition is applied on the two walls. A boundary condition with a backpressure of $2.231p_\infty$ is used at the exit of the channel [16], where $p_\infty$ is the inflow pressure. The details of the grid resolution for the computational domain are shown in Table 1.

Based on the time-dependent resolved density $\bar{\rho}$, pressure $\bar{p}$, velocity components $\tilde{u}_x$, $\tilde{u}_y$, $\tilde{u}_z$ in the $x$, $y$ and $z$ directions, where a tilde denotes the Favre filter, several average operations are introduced as follows. The symbol $\langle\phi\rangle$ means the time average and spatial average in the spanwise direction and $\{\phi\} = \langle\bar{\rho}\phi\rangle/\langle\bar{\rho}\rangle$ with a variable $\phi$. Then, their fluctuations are obtained as $\rho' = \bar{\rho} - \langle\bar{\rho}\rangle$, $p' = \bar{p} - \langle\bar{p}\rangle$ and $u_i'' = \tilde{u}_i - \{\tilde{u}_i\}$, respectively.

Fig. 2(a) shows the mean streamwise velocity distribution calculated by RANS, which is used as the inflow condition. The experimental data is also plotted for comparison. It is seen that the mean streamwise velocity is consistent with the experimental data [16].

Table 1: Details of grid resolution for computational domain.

| | grid $(N_x \times N_y \times N_z)$ | $a_\infty \Delta t/D$ | $\Delta z^+$ |
|---|---|---|---|
| Grid 1 | $1001\times 81\times 201$ | 0.0005 | $<1$ |
| Grid 2 | $801\times 61\times 181$ | 0.0005 | $<1$ |
| Grid 3 | $501\times 41\times 121$ | 0.001 | $<1$ |

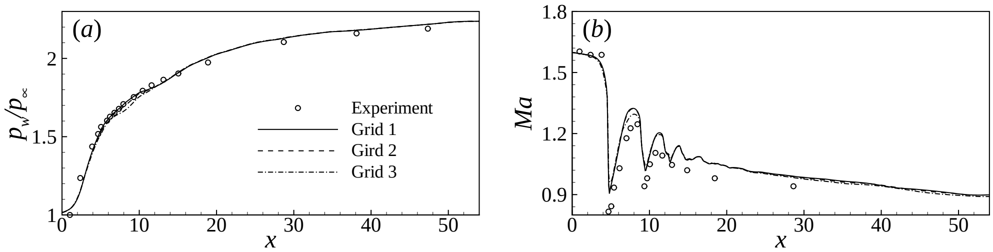


Figure 3: Comparison between the calculated results and experimental data [16]: (a) the mean pressure on the wall and (b) the mean Mach number along the centerline of the channel.

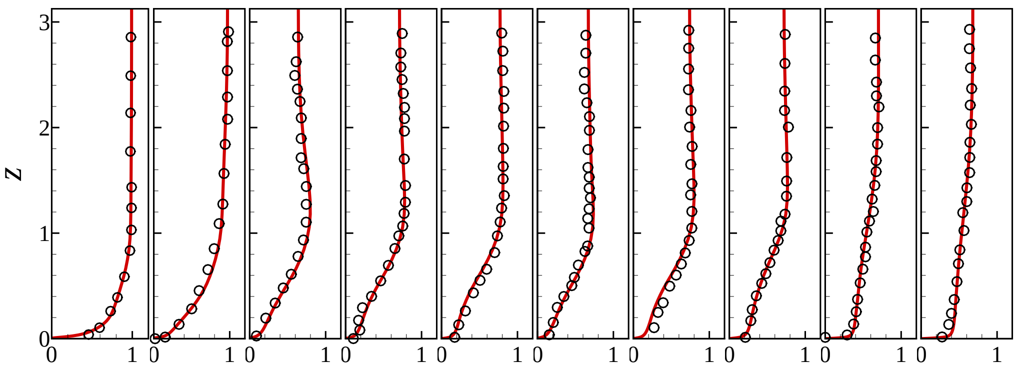


Figure 4: The streamwise velocity distribution along the vertical direction at several streamwise locations, $x=0.8$, 1.3, 2.6, 3.9, 5.3, 6.6, 8.1, 10.4, 26.2 and 35.5 from left column to right one. The symbol $\circ$ represents the experimental data [16].

The van Driest transformed streamwise velocity for the undisturbed incoming boundary layer just before the shock train is shown in Fig. 2(b). The curve exhibits a linear law near the wall and obeys log-law in the logarithmic region. The LES result [26] and the experimental data [16] are also plotted for comparison. The present result agrees well with the experimental data in the logarithmic region. As a lower Reynolds number is used in the LES study [26], the logarithmic region is shorter than our profile and the curves coincide well with each other in the viscous sublayer.

Fig. 3 shows the distributions of the mean pressure on the wall and the mean Mach number alone the centerline of the channel for comparison between numerical results and experimental data [16]. It is seen that the calculated results agree reasonably with the experimental data. To assess the effect of grid resolution and time step on the calculated results, three typical tests with different grid resolutions and time steps are listed in Table 1. As shown in Fig. 3, the results for grids 1 and 2 are consistent with each other, indicating a reasonable convergence for the grid resolution and time step. To make the prediction accurate, the results given below were calculated using the parameters for grid 1 in Table 1. Furthermore, Fig. 4 shows the streamwise velocity profiles to quantitatively compare with experimental data [16]. It is seen that the present calculated results agree well with the experimental data. Furthermore, the present numerical strategy has already been applied with success to a wide range of turbulent flows, such as compressible flow over a circular and wavy cylinder [28] and past an aerofoil [29] and supersonic flow opposing a jet from a blunt body [30].

# 3 Results and discussion

## 3.1 Statement of the flow field

The instantaneous flow structure inside the channel is shown in Fig. 5. The structure contains a series of shocks, which is called a shock train [6]. The first shock is bifurcated as a result of boundary layer separation and the following shocks exhibit nearly normal ones. The bifurcated shock consists of a leading weak oblique shock, a nearly normal outer shock and a trailing oblique shock with their intersecting at the bifurcation point, which is consistent with experimental observation [16]. The separated shear layer rolls up because of the vortical instability as the shear layer evolves downstream. Then, the fully developed turbulence exists in the downstream and the flow field no longer contains shock, where a region with adverse pressure gradient occurs as shown in Fig. 3(a) and can be referred to as "mixing region" [6].

The local flow structures based on the mean dilatation and mean local Mach number are shown in Fig. 6, where the mean flow quantities are calculated by time average and spatial average in the spanwise direction. As shown in Fig. 6(a), the shock structures are clearly demonstrated for the first bifurcated shock and the following normal shocks. The first shock creates an adverse pressure gradient, which in turn results in boundary layer separation. The separated flow region causes the formation of the leading oblique shock. The pressure has a rapid increase across the shock. As shown in Fig. 6(b), the Mach number decreases across the shock and a subsonic region exists behind the first shock. The proximity of the walls limits the flow to be parallel to the wall. The flow converge caused by the boundary layer separation induces the aerodynamic nozzle effect, which results in the acceleration of subsonic flow in the core region. The boundary layer reattaches after its separation and an expansion region forms to match the pressure difference.

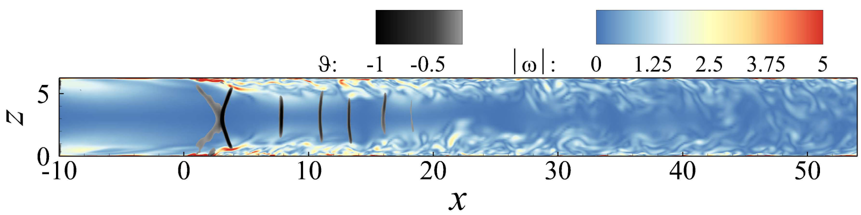


Figure 5: Instantaneous flow structures in the channel. Here, the shock structures are illustrated by contours of dilatation $\vartheta$ in grayscale. The background pattern is shown by contours of vorticity magnitude $|\omega|$.

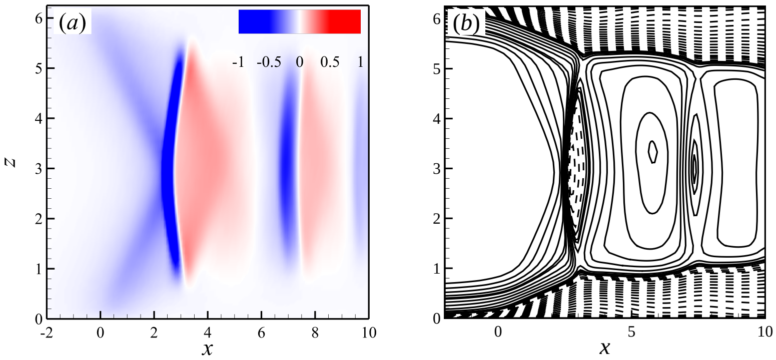


Figure 6: Local flow structures in terms of (a) the mean dilatation and (b) the mean local Mach number $Ma$. Here, solid lines denote $Ma>1$ and dashed lines $Ma<1$ with a contour increment 0.05.

## 3.2 Turbulence characteristics

### 3.2.1 Turbulence intensities and turbulent kinetic energy

Here, we mainly pay attention to the behaviors of turbulence intensities at different streamwise locations. The distributions of the normalized turbulence intensities are shown in Fig. 7. The turbulence intensity components in the near-wall region are enhanced in the multiple shock region, such as at $x=2.56$, 3.5 and 6.91, compared with that at $x=40$ in Figs. 7(a)-(c). The streamwise component at $x=2.56$ has the larger distribution in the core region of the channel due to the interaction of the first two shocks with turbulent flow. Even though the streamwise turbulence intensity at $x=40$ is lower in the near-wall region, it has a remarkable value in the core region. The spanwise and transverse turbulence intensities become more significant in the downstream. Meanwhile, the spanwise turbulence intensity at $x=40$ is larger, which is associated with the evolution of vortical structures. As shown in Fig. 5, the spanwise vortical structures become unstable and the streamwise vortices strengthen gradually, resulting in the enhancement of the spanwise velocity fluctuation. Further, the transverse turbulence intensity at $x=2.56$ has an obvious increase, which is related to the shock/boundary layer interaction.

The distributions of the normalized pressure fluctuation are also shown in Fig. 7(d). The pressure fluctuation is significantly enhanced in the multiple shock region. This behavior is consistent with the turbulence intensities. The profiles at $x=2.56$ and 6.91, corresponding to the first two shocks, exhibit a sharp increase in the core region because the shock may enhance the pressure fluctuation.

The distributions of the specific turbulent kinetic energy (TKE) are shown in Fig. 8. As noticed in the investigation of shock wave/boundary layer interaction [38], a spatially evolving turbulent compressible boundary layer exhibits a similarity with the incompressible case. The turbulent kinetic energy for incompressible boundary layer obeys the near-wall asymptotic behavior $k\simeq A_k z^2$ [39, 40], where $A_k$ is a constant. Therefore, the illustrated slope in Fig. 8 indicates that the present calculation can reliably simulate the

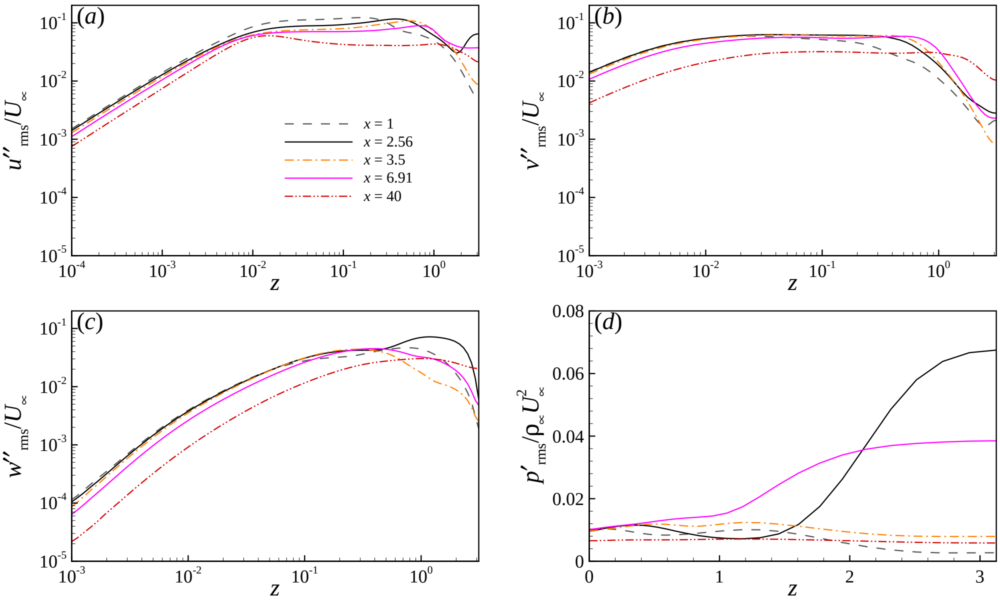


Figure 7: The transverse distributions of turbulence intensities at several streamwise locations for the (a) streamwise, (b) spanwise and (c) transverse turbulence intensity and (d) pressure fluctuation. The selected streamwise locations are described as follows. The first shock locates at $x=2.56$ and the second one at $x=6.91$. The position $x=1$ lies in front of the first shock, $x=3.5$ behind the first shock and $x=40$ in the downstream.

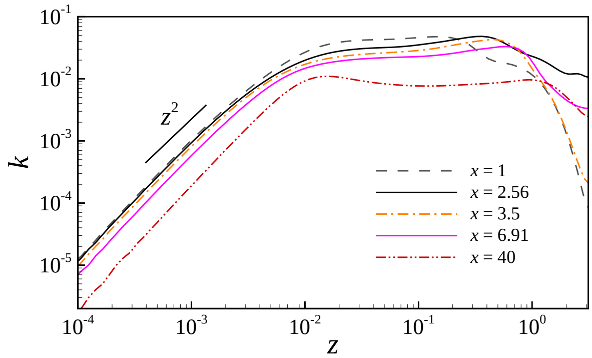


Figure 8: The transverse distributions of the specific turbulent kinetic energy at several streamwise locations. For details see Fig. 7.

turbulence behavior.

Further, as shown in Fig. 8, the TKE in the near-wall region has an obvious enhancement in the multiple shock region. It is seen that the TKE has relatively high level at the first shock location and the TKE at $x=1$ and 3.5 has a similar order to that at $x=2.56$. The second shock at $x=6.91$ also makes a remarkable contribution to the TKE, which is somewhat smaller than the first one due to the weakening of the second shock. Moreover, the

TKE in the core region exhibits relatively higher value in the downstream of the channel, corresponding to the fully developed turbulence.

#### 3.2.2 Budget terms in the turbulent kinetic energy transport equation

The budget terms in the TKE transport equation, which have been normalized based on the free-stream quantities [41], are further discussed. Fig. 9 shows the transverse distributions of the TKE production term. The production term at the first shock position has a peak in the core region, corresponding to the TKE peak in Fig. 8. This indicates that the unsteadiness of the shock can promote the TKE production. The production term also has the local peaks for the downstream shocks, which decrease due to the weakening of the shocks. The production term at $x=1$ has a peak in the near-wall region, which is related to the shearing effect induced by turbulent boundary layer. The peak shifts away from the wall at $x=2.56$, corresponding to the boundary layer separation. This behavior indicates that the shearing effect has an important promotion to the TKE production. Moreover, the production term at $x=3.5$ becomes negative, which is associated with the expansion effect after the first shock.

Further, the TKE production term can be decomposed into two parts, which are related to the compressing and shearing processes [42,43],

$$P_d=-\frac{1}{3}\langle\bar{\rho}u''_iu''_i\rangle\frac{\partial\{\tilde{u}_j\}}{\partial x_j}, \tag{3.1a}$$

$$P_s=-\left(\langle\bar{\rho}u''_iu''_j\rangle-\frac{1}{3}\langle\bar{\rho}u''_iu''_i\rangle\delta_{ij}\right)\frac{\partial\{\tilde{u}_j\}}{\partial x_j}, \tag{3.1b}$$

where $P_d$ is the part due to the correlation between the dilatation and the isotropic component of the Reynolds stresses and $P_s$ is the part due to the correlation between the deformation strain and the anisotropic part of the Reynolds stresses. Fig. 10 shows the distribution of the TKE production terms due to the dilatation and shear contribution. The

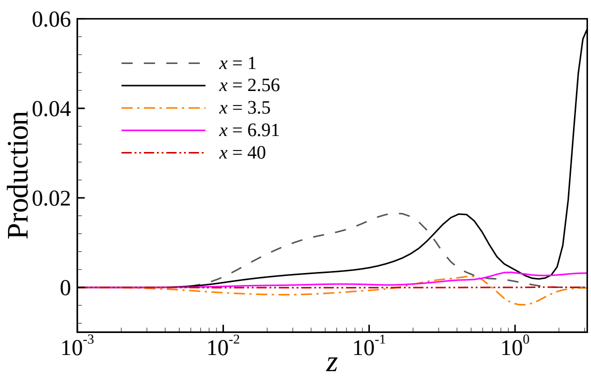


Figure 9: The transverse distributions of the TKE production at several streamwise locations. For details see Fig. 7.

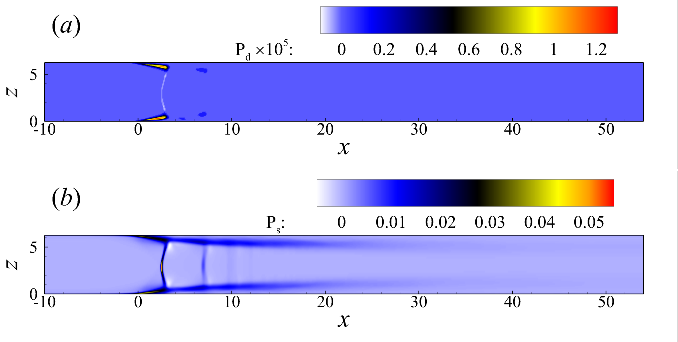


Figure 10: Distribution of the TKE production terms: (a) dilatation production $P_d$; (b) shear production $P_s$.

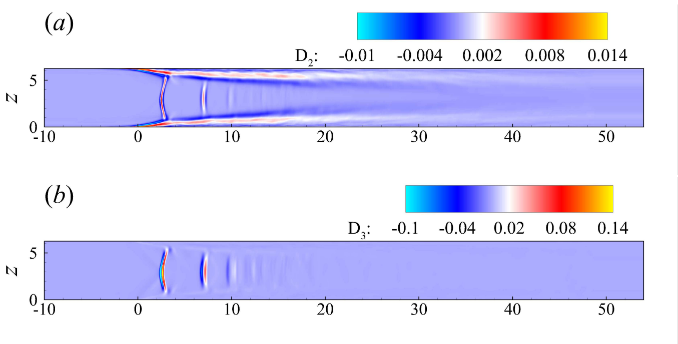


Figure 11: Distribution of turbulent diffusion: (a) diffusion due to the triple velocity correlation; (b) diffusion due to the pressure-velocity correlation.

dilatation production $P_d$ has positive distribution in the compression region and negative one in the expansion region [42,43]. As shown in Fig. 10(a), the dilatation production $P_d$ is positive at the ramp of separation region, which results in an increase of the TKE. Then, $P_d$ is negative behind the first shock for the existence of the expansion waves, which leads to a decrease of the TKE. The distribution of the shear production $P_s$ is shown in Fig. 10(b). The shear production $P_s$ remarkably distributes in the regions where the shear layers and the shocks occur. Even though the dilatation production $P_d$ is enhanced by the shocks, it remains smaller with respect to the shear production $P_s$. Therefore, the production is still dominated by the shear production $P_s$.

The turbulent diffusion is further analyzed and can be divided into three parts, including the viscous effect $D_1 = \langle \tau''_{ij} u''_i \rangle_{,j}$ , the triple velocity correlation $D_2 = -\langle \bar{\rho} u''_i u''_i u''_j / 2 \rangle_{,j}$ and the pressure-velocity correlation $D_3 = -\langle \rho'_{\ i} u''_j \rangle_{,j}$ [29]. Fig. 11 shows the distribution of the turbulent diffusion terms. The diffusion due to the viscous effect mainly concentrates the near-wall region which is not shown here. Fig. 11(a) shows the distribution of the turbulent diffusion due to the triple velocity correlation. This part mainly concentrates in the regions where the shocks and separated shear layers

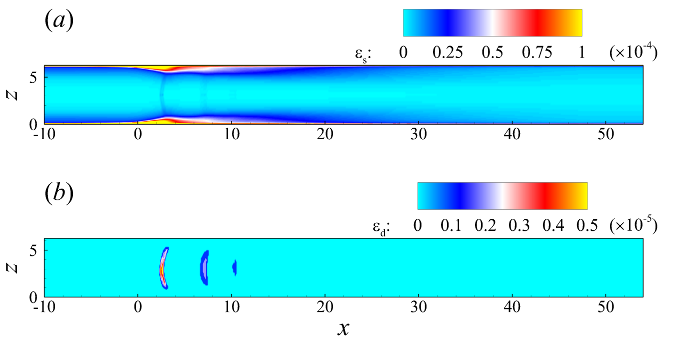


Figure 12: Distribution of the turbulent dissipation rate: (a) solenoidal part, (b) dilatational part.

occur, which exhibits negative distribution in front of and behind the shock. As shown in Fig. 11(b) for the pressure-velocity correlation, it mainly distributes in the region of shocks, because the pressure and velocity have a remarkable change across the shocks and the unsteadiness of the shocks also strengthens the pressure and velocity fluctuations. Compared the $D_2$ and $D_3$ parts, it is identified that the turbulent diffusion is mainly dominated by the pressure-velocity correlation part and concentrates in the region of shocks.

We further examine the turbulent dissipation rate $\varepsilon$, which can be separated into a solenoidal part $\varepsilon_s$ and a dilatational part $\varepsilon_d$ [44,56],

$$\begin{aligned}\varepsilon=&\varepsilon_s+\varepsilon_d=\langle\tau''_{ij}u''_{i,j}\rangle\\=&\Big\langle\frac{\tilde{\mu}}{Re}\omega''_i\omega''_i+2\frac{\tilde{\mu}}{Re}\big(u''_{i,j}u''_{j,i}-(u''_{i,i})^2\big)\Big\rangle+\frac{4}{3}\Big\langle\frac{\tilde{\mu}}{Re}(u''_{i,i})^2\Big\rangle,\end{aligned}\tag{3.2}$$

where $\omega''_i$ denotes the fluctuating vorticity vector and $\tilde{\mu}$ the molecular viscosity.

Here, Fig. 12 shows the solenoidal and the dilatational part of the turbulent dissipation rate. The dilatation part $\varepsilon_d$ in Fig. 12(a) is a pure compressibility effect [29] and mainly concentrates in the multiple shock region. The solenoidal part $\varepsilon_s$ in Fig. 12(b) is largely independent of the compressibility [45] and mainly exists in the shear layer region. Moreover, we can identify that the solenoidal part $\varepsilon_s$ dominates the turbulent dissipation, consistent with previous findings [29,46]. This behavior indicates that the separated shear layers and the vortical structures in the flow field play a dominant role on the turbulent dissipation.

### 3.2.3 Production of the pressure fluctuation

From the preceding discussion, the pressure fluctuation is significantly generated in the multiple shock region. Based on the transport equation of the pressure fluctuation $\langle p'^2\rangle$ [47,48], we can have a deep insight into the understanding of the pressure fluctuation production. Here the production term $P_{pf}$ is mainly analyzed which is represented

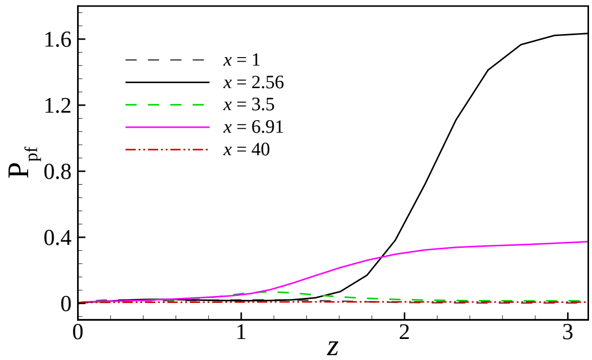


Figure 13: The transverse distributions of the production term of the pressure fluctuation equation at several streamwise locations. For details see Fig. 7.

as [48]

$$P_{pf}=-2\langle p'u'_i\rangle\frac{\partial\langle\bar{p}\rangle}{\partial x_i}-2\gamma\langle p'^2\rangle\tilde{\vartheta}+2(\gamma-1)(\langle p'\tau'_{ij}\rangle\langle S_{ij}\rangle+\langle p'S'_{ij}\rangle\langle\tau_{ij}\rangle), \tag{3.3}$$

where $\gamma$ is the ratio of the specific heats, $S_{ij}=(\partial u_i/\partial x_j+\partial u_j/\partial x_i)/2$ is the strain-rate tensor, $\tau_{ij}=2\tilde{\mu}(S_{ij}-\vartheta\delta_{ij}/3)$ is the viscous-stress tensor and $\tilde{\vartheta}=\partial\{\tilde{u}_i\}/\partial x_i$.

The transverse distribution of the production term $P_{pf}$ is shown in Fig. 13. The production of the pressure fluctuation at $x=2.56$ varies smoothly for $z<1.5$ and then has a significant increase due to the interaction between the shock and separated boundary layer. The profile at the second shock position exhibits a smooth variation owing to the weaker interaction between the shock and boundary layer. In addition, the production in the core region has a larger peak at the first shock position and decreases for the following shocks due to the weakening of these shocks. Moreover, the profile of the production behind the first shock at $x=3.5$ is similar to that in the downstream at $x=40$. This behavior indicates that the unsteadiness of the shocks can strengthen the pressure fluctuation.

### 3.3 Feature of the shear layer evolution

The shear layer evolution has a remarkable influence on the production and diffusion of the turbulence and on the unsteady feature of the flow field. Thus, the features of the shear layer evolution are further investigated in order to get into the understanding of the flow behaviors.

To identify the shear layer, the contour of the turbulent shear stress $\tau''_{xz}=\{u''_x u''_z\}$ is shown in Fig. 14. The shear layer near the lower wall is typically analyzed. It is seen that the $\tau''_{xz}$ mainly occurs in the boundary layer region. For the purpose of better understanding the shear layer evolution, the location of the shear layer is determined in terms of local peak of the shear stress magnitude [30, 49, 50], which is exhibited by the dashed line marked in Fig. 14.

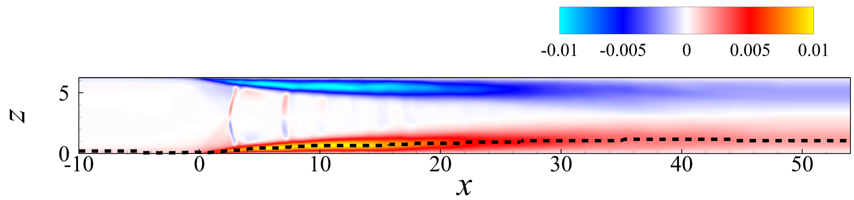


Figure 14: Distribution of the turbulent shear stress $\tau''_{xz}$. Here the black dashed line is the location of the local peak shear stress magnitude which can be used to denote the shear layer location.

Fig. 15 shows the distribution of the mean dilatation $\vartheta$ and the streamwise gradient of mean entropy along the centerline of the channel and the shear layer marked in Fig. 14, respectively. The entropy increases across the shock, achieves its maximum at the shock position and then decreases behind the shock. In comparison with other variables such as the density, pressure, velocity and temperature in the flow field, the streamwise gradient of entropy can be used to distinguish the shock position. On the other hand, the velocity gradient also exhibits a sharp change across the shock. Therefore, the distribution of the dilatation can be also utilized as the identification of the shock.

As shown in Fig. 15(a), the distribution of the mean dilatation along the centerline exhibits its negative peak at the first four shock positions. Correspondingly, the streamwise gradient of entropy along the centerline also shows its peak. The positions for the first four shocks can be determined as approximately $x=2.56$, 6.91, 9.76 and 12, respectively. From Fig. 15(b), the distributions of the dilatation and the streamwise gradient of entropy along the shear layer have the similar behavior to those along the centerline. Meanwhile, the dilatation along the shear layer has two adjacent negative peaks, which locate at $x=0.55$ and 2.81, respectively, corresponding to the two bifurcated ends of the first shock. The steamwise gradient of entropy also exhibits two peaks. Owing to the weakening of the following shocks, the streamwise gradient of entropy has no longer obvious peaks in the downstream.

The distributions of the TKE and pressure fluctuation along the shear layer are shown in Fig. 16. The first two peaks of the TKE along the shear layer in Fig. 16(a) locate at $x=0.55$ and 2.81, which are related to the interaction between the bifurcated ends of the first shock and the shear layer. The TKE enhancement is caused by the unsteadiness of the separated shear layer and multiple shock. Because of the weakening of the following shocks, the TKE keeps decaying along the shear layer. The distribution of TKE along the centerline is also plotted in Fig. 16(a) for comparison. The TKE has two obvious peaks at the first two shocks and exhibits relatively lower level at other shock positions. In addition, the TKE along the centerline is obviously lower compared with that along the shear layer. The distribution of the pressure fluctuation $p'_{rms}$ along the shear layer and the centerline is shown in Fig. 16(b). The pressure fluctuation along the shear layer has a sharp increase owing to the shear layer separation, increases gradually in the shock train region and then decreases slightly in the downstream. The pressure fluctuation along the

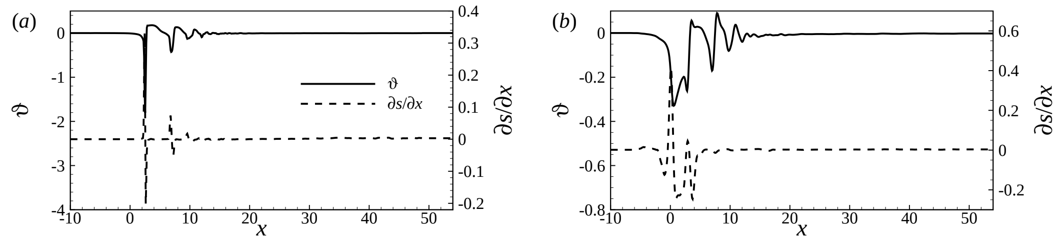


Figure 15: The distributions of the mean dilatation and the streamwise gradient of entropy along (a) the centerline and (b) the shear layer.

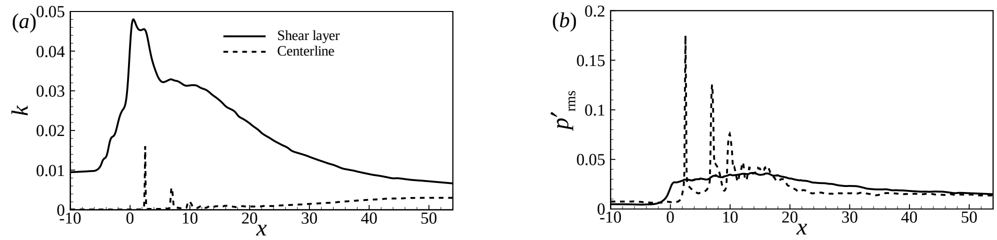


Figure 16: The distributions of (a) the TKE and (b) the pressure fluctuation $p'_{rms}$ along the centerline of the channel and the shear layer.

centerline has the similar level to that along the shear layer and its peaks can be observed at the multiple shock position.

### 3.4 Unsteady property of flow structures

The flow structures including the multiple shock and the separated shear layer play an important role in the statistical properties of the flow field. Further, the unsteady property of these flow structures is investigated in terms of the power spectral analysis and the proper orthogonal decomposition (POD) method.

The pressure power spectral analysis in the turbulent flow is helpful for the understanding of the turbulence structures [51–53]. Fig. 17 exhibits the distributions of the pressure power spectral density (PSD) at three typical probes. As shown in Fig. 17(a), the PSD at the first probe has a peak at $St=0.0124$, which corresponds to the oscillation of the second shock. There exist other two peaks at $St=0.0309$ and 0.0433. Then, the dominant frequency for the second probe in Fig. 17(b) is $St=0.0309$. Further, the dominant frequency for the third probe in Fig. 17(c) also exhibits $St=0.0309$, which corresponds to the roll-up vortices of the shear layer. Meanwhile, another peak at $St=0.0433$ occurs due to the linear combination of $St=0.0124$ and 0.0309, which is reasonably related to the interaction between the shock and shear layer.

The pressure field can be quantitatively analyzed using the POD method [54] to extract energetic coherent structures from the simulation data. For a given pressure field $p(\mathbf{x},t)$, the POD analysis can determine a set of orthogonal functions $\phi_j(\mathbf{x})$, $j=1,2,\cdots$, so

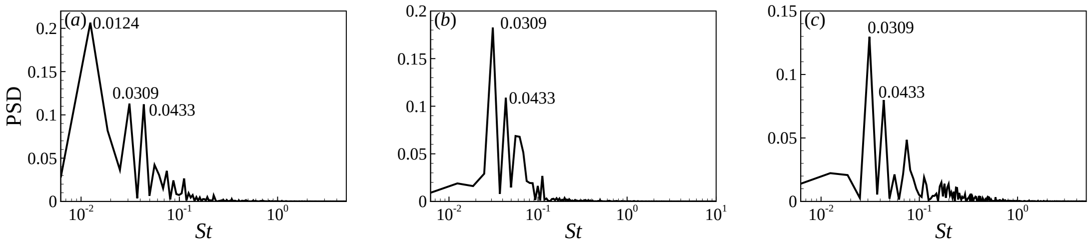


Figure 17: Profiles of the pressure PSD at three probes: (a) the first probe locates at (6.5,3.125) just in front of the second shock along the centerline, (b) the second one at (11,3.125) between the third and the fourth shocks and (c) the third one at (11,1), where the fourth shock interacts with the shear layer.

that projection of $p$ on to the first $n$ functions,

$$\hat{p}(\mathbf{x},t)=\bar{p}(\mathbf{x},t)+\sum_{j=1}^{n}a_j(t)\phi_j(\mathbf{x}), \tag{3.4}$$

has the smallest error, defined as $\langle\|p-\hat{p}\|^2\rangle_t$, where $\langle\cdot\rangle_t$ and $\|\cdot\|$ denote the time average and a norm in the $L^2$ space, respectively. Here, $a_j(t)$ represents the temporal variation of the $j$th mode.

The analysis has been conducted using $N_t=3000$ snapshots of the pressure field, which span a time period of $150\delta/U_\infty$ with the temporal resolution of $0.05\delta/U_\infty$. The energy of the $j$th mode $E_j$ is defined as

$$E_j=\left\langle\|a_j(t)\phi_j(x)\|^2\right\rangle_t. \tag{3.5}$$

The normalized energy of the $m$th mode is then defined as $E_m/\sum_{j=1}^{N_t}E_j$ and the energy sum from mode 1 through to mode $m$ is solved as $\sum_{j=1}^{m}E_j/\sum_{j=1}^{N_t}E_j$. Using the time-varying coefficient $a_j(t)$ in (3.4), one can obtain the frequency spectrum of the $j$th mode [29,55].

Fig. 18 shows the shape distributions and the corresponding frequency spectra for the first three modes. The pressure fluctuation for the first mode in Fig. 18(a) exhibits alternating patterns of positive and negative pressure fluctuation near the wall, which corresponds to the roll-up vortices of the shear layer. Obvious fluctuation is also observed in the regions where the shocks occur. As shown in Figs. 18(b) and 18(c) for the second and third modes, the pressure fluctuation mainly concentrates in the multiple shock region, which is related to the oscillation of the shocks. From the time-varying coefficient of mode 1, the dominant frequency is approximately $St=0.0309$, which corresponds to the frequency of the roll-up vortices of the shear layer. Meanwhile, the dominant frequency of modes 2 and 3 is approximately $St=0.0124$, which is consistent with the frequency of the shock oscillation. Further, as shown in Fig. 19(a), the first three modes occupy 10.4%, 9.6% and 8.5%, respectively. The total energy of the first three mode occupies 28.5% in Fig. 19(b). Based on the POD analysis, the dominant coherent structures related

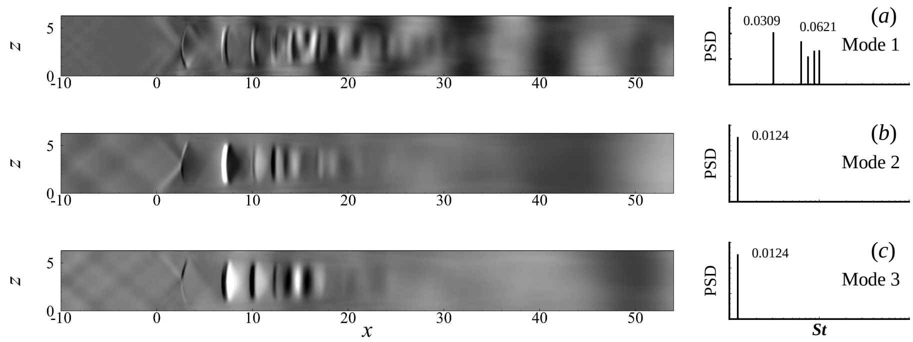


Figure 18: Spatial distributions of the first three POD modes and power spectra of their time-varying coefficients: (a) mode 1 and its spectra, (b) mode 2 and its spectra and (c) mode 3 and its spectra. The contour levels ranges from $-0.01\rho_\infty U_\infty^2$ to $0.01\rho_\infty U_\infty^2$.

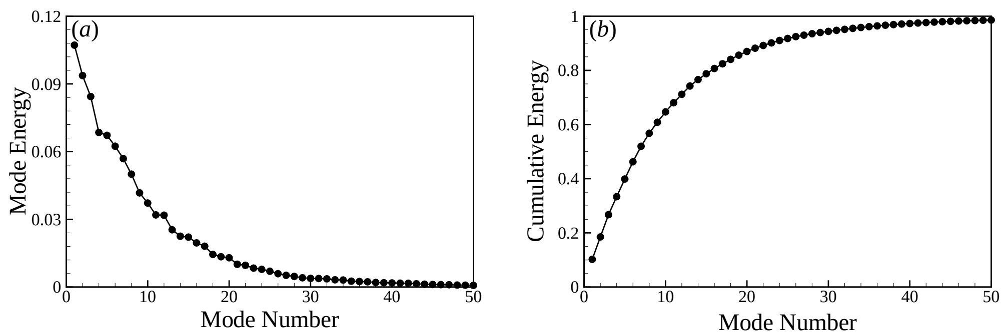


Figure 19: Energy distribution of the first fifty POD modes based on the pressure fluctuation for (a) the mode energy and (b) cumulative energy.

to the pressure fluctuation are reasonably determined and the dominant frequencies for the multiple shock and the shear layer evolution are identified.

## 4 Concluding remarks

Multiple shock/turbulent flow interaction in a supersonic channel has been studied by means of an LES technique for the inlet free-stream Mach number $M_{in}=1.61$ and the unit Reynolds number $1.62\times10^5$ based on the 99% velocity thickness. Various fundamental mechanisms dictating the complex flow phenomena including shock train, shear layer and turbulence behavior are examined in detail and are summarized briefly as follows.

The shock train or multiple shock structure is reliably simulated. The typical flow structures in the flow field include multiple shock, separated shear layer and multiple shock/turbulent flow interaction. Due to the existence of the multiple shock, an obvious increase of the pressure on the wall occurs in the multiple shock region and a decrease of the Mach number along the centerline appears. The existence of the multiple shock and separated shear layer has a significant influence on the turbulence features. It is found that the turbulence intensities and the TKE are enhanced by the unsteadiness of the shocks and weakened in the downstream of the channel. The unsteadiness of the shocks also strengthens the pressure fluctuation. Moreover, the pressure-velocity correlation plays a dominant role in the turbulence diffusion and mainly concentrates in the multiple shock region. The separated shear layer has a major contribution to the turbulence dissipation. The analysis on the transport equation of the pressure fluctuation reveals that the multiple shock mainly induces the pressure fluctuation. The unsteady behavior of the flow field is further investigated. It is found that the multiple shock and the separated shear layer dominate the unsteady features of the flow field.

## Acknowledgements

This work was supported by Science Challenge Project (No. TZ2016001) and by the National Natural Science Foundation of China (Nos. 11572312 and 11621202).

## References

[1] S. Priebe, M. Wu and M. P. Martin, *Direct numerical simulation of a reflected-shock-wave/turbulent-boundary-layer interaction*, AIAA J., 47 (2009), pp. 1173–1185.

[2] S. Pirozzoli and M. Bernardini, *Direct numerical simulation database for impinging shock wave/turbulent boundary-layer interaction*, AIAA J., 49 (2011), pp. 1307–1312.

[3] B. Morgan, K. Duraisamy, N. Nguyen, S. Kawai and S. K. Lele, *Flow physics and RANS modelling of oblique shock/turbulent boundary layer interaction*, J. Fluid Mech., 729 (2013), pp. 231–284.

[4] M. Wu and M. P. Martin, *Direct numerical simulation of supersonic turbulent boundary layer over a compression ramp*, AIAA J., 45 (2007), pp. 879–889.

[5] D. Dawson, S. Kawai and S. K. Lele, *Large-eddy simulation of a Mach 2.9 turbulent boundary layer over a* $24^\circ$ *compression ramp*, AIAA Paper, (2011), pp. 2011–3431.

[6] K. Matsuo, Y. Miyazato and H.-D. Kim, *Shock train and pseudo-shock phenomena in internal gas flow*, Prog. Aerosp. Sci., 35 (1999), pp. 33–100.

[7] T. Ikui, K. Matsuo, M. Nagai and M. Honjo, *Oscillation phenomena of pseudo-shock waves*, Bull. JSME, 17 (1974), pp. 1278–1285.

[8] T. Ikui, K. Matsuo and K. Sasaguchi, *Modified diffusion model of pseudo-shock waves considering upstream boundary layers*, Bull. JSME, 24 (1981), pp. 1920–1927.

[9] R. Yamane, E. Kondo, Y. Tomita and N. Sakae, *Vibration of pseudo-shock in straight duct: 1st report, fluctuation of static pressure*, Bull. JSME, 27 (1984), pp. 1385–1392.

[10] R. Yamane, M. Takahashi and N. Sakae, *Vibration of pseudo-shock in straight duct: 2nd report, calculation of static pressure fluctuation*, Bull. JSME, 27 (1984), pp. 1393–1398.

[11] H. Sugiyama, H. Takeda, J. Zhang, K. Okuda and H. Yamagishi, *Locations and oscillation phenomena of pseudo-shock waves in a straight rectangular duct*, JSME Int. J., 31 (1988), pp. 9–15.

[12] E. P. Neumann and F. Lustweak, *Supersonic diffusers for wind tunnels*, J. Appl. Mech., 16 (1949), pp. 195–202.

[13] J. LUKASIEWICZ, *Diffusers for supersonic wind tunnels*, J. Appl. Mech., 20 (1953), pp. 617–626.
[14] A. H. SHAPIRO, The Dynamics and Thermodynamics of Compressible Fluid Flow, Ronald Press, (1953).
[15] B. F. CARROLL AND J. C. DUTTON, *Characteristics of multiple shock wave/turbulent boundary-layer interactions in rectangular ducts*, J. Propul. Power, 6 (1990), pp. 186–193.
[16] B. F. CARROLL AND J. C. DUTTON, *Multiple normal shock wave/turbulent boundary-layer interactions*, J. Propul. Power, 8 (1992), pp. 441–448.
[17] B. F. CARROLL AND J. C. DUTTON, *Turbulence phenomena in a multiple normal shock wave/Turbulent boundary-layer interaction*, AIAA J., 30 (1992), pp. 43–48.
[18] B. F. CARROLL, P. A. LOPEZ-FERNANDEZ AND J. C. DUTTON, *Computations and experiments for a multiple normal shock/boundary-layer interaction*, J. Propul. Power, 9 (1993), pp. 405–411.
[19] I. HATAUE, *Computational study of the shock-wave/boundary-layer interaction in a duct*, Fluid Dynam. Res., 5 (1989), pp. 217–234.
[20] P. LIN, *Geometric effects on precombustion shock train in constant area isolators*, AIAA Paper, (1993), pp. 93–1838.
[21] R. YAMANE, S. OSHIMA, Y. NAKAMURA, T. ISHII AND M. K. PARK, *Numerical simulation of pseudoshock in straight channels*, JSME Int. J., 38 (1995), pp. 549–554.
[22] C. D. LINDSTROM, D. DAVIS AND S. WILLIAMS, *Shock-train structure resolved with absorption spectroscopy part 1: System design and validation*, AIAA J., 47 (2009), pp. 2368–2378.
[23] C. D. LINDSTROM, D. DAVIS AND S. WILLIAMS, *Shock-train structure resolved with absorption spectroscopy part 2: Analysis and CFD comparison*, AIAA J., 47 (2009), pp. 2379–2390.
[24] J. A. BOLES, J.-I. CHOI AND J. R. EDWARDS, *Simulations of high-speed internal flows using LES/RANS models*, AIAA Paper, (2009), pp. 09–1324.
[25] H. KOO AND V. RAMAN, *Large-eddy simulation of a supersonic inlet-isolator*, AIAA J., 50 (2012), pp. 1596–1613.
[26] B. MORGAN, K. DURAISAMY AND S. K. LELE, *Large-eddy simulations of a normal shock train in a constant-area isolator*, AIAA J., 52 (2014), pp. 539-558.
[27] X.-Y. LU, S.-W. WANG, S.-W. SUNG, S. Y. HSIEH AND V. YANG, *Large-eddy simulations of turbulent swirling flows injected into a dump chamber*, J. Fluid Mech., 527 (2005), pp. 171–195.
[28] C.-Y. XU, L.-W. CHEN AND X.-Y. LU, *Large-eddy simulation of the compressible flow past a wavy cylinder*, J. Fluid Mech., 665 (2010), pp. 238–273.
[29] L.-W. CHEN, C.-Y. XU AND X.-Y. LU, *Numerical investigation of the compressible flow past an aerofoil*, J. Fluid Mech., 643 (2010), pp. 97–126.
[30] L.-W. CHEN, G.-L. WANG AND X.-Y. LU, *Numerical investigation of a jet from a blunt body opposing a supersonic flow*, J. Fluid Mech., 684 (2011), pp. 85–110.
[31] N. D. SANDHAM, Y.-F. YAO AND A. A. LAWAL, *Large-eddy simulation of transonic turbulent flow over a bump*, Intl J. Heat Fluid Flow, 524 (2003), pp. 584–595.
[32] Q. LI AND G. N. COLEMAN, *DNS of an oblique shock wave impinging upon a turbulent boundary layer*, In Direct and Large-Eddy Simulation V, 9 (2003), pp. 387–396.
[33] S. PIROZZOLI, M. BERNARDINI AND F. GRASSO, *Characterization of coherent vortical structures in a supersonic turbulent boundary layer*, J. Fluids Mech., 613 (2008), pp. 205–231.
[34] S. PIROZZOLI, M. BERNARDINI AND F. GRASSO, *Direct numerical simulation of transonic shock/boundary layer interaction under conditions of incipient separation*, J. Fluids Mech., 657 (2010), pp. 361–393.
[35] S. PIROZZOLI, M. BERNARDINI AND F. GRASSO, *On the dynamical relevance of coherent vortical structures in turbulent boundary layer*, J. Fluids Mech., 648 (2010), pp. 325–349.
[36] L. WANG AND X.-Y. LU, *Flow topology in compressible turbulent boundary layer*, J. Fluids Mech.,

703 (2012), pp. 255–278.
[37] G. MATHEOU, A. M. BONANOS, C. PANTANO AND P. E. DIMOTAKIS, *Large-eddy simulation of mixing in a recirculating shear flow*, J. Fluids Mech., 646 (2010), pp. 375–414.
[38] S. PIROZZOLI AND F. GRASSO, *Direct numerical simulation of impinging shock wave/turbulent boundary layer interaction at $M=2.25$*, Phys. Fluids, 18 (2006), 065113.
[39] V. C. PATEL, W. RODI AND G. SCHEUERER, *Turbulence models for near-wall and low Reynolds number flows: a review*, AIAA J., 23 (1985), pp. 1308–1319.
[40] C. G. SPEZIALE, R. ABID AND E. C. ANDERSON, *Critical evaluation of two-equation models for near-wall turbulence*, AIAA J., 30 (1992), pp. 324–331.
[41] W. SHYY AND V. S. KRISHNAMURTY, *Compressible effects in modeling complex turbulent flow*, Prog. Aerosp. Sci., 33 (1997), pp. 587–645.
[42] J. GAVIGLIO, J. P. DUSSAUGE, J. F. DEBIEVE AND A. FAVRE, *Behavior of a turbulent flow, strongly out of equilibrium, at supersonic speeds*, Phys. Fluids, 20 (1977), pp. 179–192.
[43] F. GÉNIN AND S. MENON, *Studies of shock/turbulent shear layer interaction using large-eddy simulation*, Comput. Fluids, 39 (2010), pp. 800–819.
[44] O. ZEMAN, *Dilatation dissipation: the concept and application in modelling compressible mixing layers*, Phys. Fluids A, 2 (1990), pp. 178–188.
[45] S. K. LELE, *Compressibility effects on turbulence*, Annu. Rev. Fluid Mech., 26 (1994), pp. 211–254.
[46] B. VREMAN, H. KUERTEN AND B. GEURTS, *Shocks in direct numerical simulation of the confined three-dimensional mixing layer*, Phys. Fluids, 7 (1995), pp. 2105–2107.
[47] R. LECHNER, J. SETERHENN AND R. FRIEDRICH, *Turbulent supersonic channel flow*, J. Turbul., 2 (2001), pp. 1–25.
[48] G. A. GEROLYMOS AND I. VALLET, *Pressure, density, temperature and entropy fluctuations in compressible turbulent plane channel flow*, J. Fluid Mech., 757 (2014), pp. 701–746.
[49] J. L. HERRIN AND J. C. DUTTON, *The turbulence structure of a reattaching axisymmetric compressible free shear layer*, Phys. Fluids, 9 (1997), pp. 3502–3512.
[50] F. SIMON, S. DECK, P. GUILLEN, P. SAGAUT AND A. MERLEN, *Numerical simulation of the compressible mixing layer past an axisymmetric trailing edge*, J. Fluid Mech., 591 (2007), pp. 215–253.
[51] B. E. MCGRATH AND R. L. SIMPSON, *Same features of surfaces pressure fluctuations in turbulent boundary layers with zero and favorable pressure gradient*, NASA CR, (1987), pp. 606–613.
[52] R. L. SIMPSON, M. GHODBANE AND B. E. MCGRATH, *Surface pressure fluctuations in a separating turbulent boundary layer*, J. Fluid Mech., 177 (1987), pp. 167–186.
[53] Y. NA AND P. MOIN, *The structure of wall-pressure fluctuations in turbulent boundary layers with adverse pressure gradient and separation*, J. Fluid Mech., 377 (1998), pp. 347–373.
[54] G. BERKOOZ, P. HOLMES AND J. L. LUMLEY, *The proper orthogonal decomposition in the analysis of turbulent flows*, Annu. Rev. Fluid Mech., 25 (1993), pp. 539–575.
[55] J. K. WANG AND M. SUN, *A computational study of the aerodynamics and forewing-hindwing interaction of a model dragonfly in forward flight*, J. Exp. Biol., 208 (2005), pp. 3785–3805.
[56] S. SARKAR, G. ERLEBACHER, M. Y. HUSSAINI AND H. O. KREISS, *The analysis and modelling of dilatational terms in compressible turbulence*, J. Fluid Mech., 227 (1991), pp. 473–493.